A VLT/FORS2 NARROWBAND IMAGING SEARCH FOR MG II EMISSION AROUND $z \sim 0.7$ GALAXIES

Ryan Rickards Vaught,[1,2] Kate H. R. Rubin,[1] Fabrizio Arrigoni Battaia,[3] J. Xavier Prochaska,[4] and Joseph Hennawi[5]

[1] Department of Astronomy, San Diego State University, San Diego, CA 92182

[2] Center for Astrophysics and Space Sciences, Department of Physics, University of California, San Diego, CA

[3] Max-Planck-Institut fur Astronomie, Konigstuhl 17, D- 69117 Heidelberg, Germany

[4] Astronomy & Astrophysics, UC Santa Cruz, 1156 High St., Santa Cruz, CA 95064 USA

[5] Department of Physics, Broida Hall, University of California, Santa Barbara, CA 93106-9530

ABSTRACT

The mass and energy of galactic winds remain poorly constrained via traditional absorption line studies. One way to better constrain these parameters is to measure the spatial extent of the outflow in emission. We perform a VLT/FORS2 narrowband imaging of 5 star-forming galaxies at redshift $z = 0.67 - 0.69$ in the GOODS-S field as part of an effort to spatially resolve and constrain the radial extent of large-scale outflows traced by Mg II emission. These observations probe extended Mg II emission down to unmatched surface brightness limits of 5.74×10^{-19} ergs sec $^{-1}$ cm^{-2} arcsec^2 (5σ). We do not detect any extended Mg II emission in any of our galaxies, thus placing strong upper limits on the strength of Mg II emission in the sample galaxies. Our observations allow us to create the first ever spatially-resolved map of Mg II absorption, revealing approximately constant absorption strengths across the galaxy disks. Our detection limits in concert with a previous studies Keck/LRIS spectra allow us to model Mg II emission for isotropic and anisotropic dust-free winds. We find that anisotropic winds reduce the strength of estimated missing Mg II emission below our 5σ limit.

Keywords: galaxies: evolution, Galactic Winds

1. INTRODUCTION

Galactic winds play a critical role in regulating the star formation rates and stellar masses of galaxies (Werk et al. 2014); however, the physical mechanism that powers these galactic winds remains uncertain. Some possible mechanics have been proposed by theoretical studies that include thermal pressure from core collapse supernova, radiation pressure from starbursts and finally cosmic ray pressure (Larson 1974; Chevalier & Clegg 1985; Springel & Hernquist 2003; Sugahara et al. 2017). However it is very difficult to distinguish between these mechanisms with current observational techniques. Additionally, the impact galactic winds have on their host galaxies (i.e, their mass and energy content) has remained difficult to constrain with observations.

Corresponding author: Ryan Rickards Vaught
rjrickar@ucsd.edu

An accurate picture of what types of galaxies host outflows comes from numerous absorption line studies of galaxies (Veilleux et al. 2005; Weiner et al. 2009; Martin et al. 2012; Rubin et al. 2014). Outflows are detected by measuring the blueshift (outflow) or redshift (inflow) of absorption transitions with respect to the host galaxy systematic velocities. Spectroscopy of galaxies from low to high redshifts probing cold gas which absorbs in Na I and cool gas in Mg II has revealed outflows in most galaxies that host active star-formation (e.g. Martin et al. 2012; Rubin et al. 2014). Even though these probes can ascertain: the radial velocity, column density and covering fraction of the flow, this method is weak in constraining the overall radial extent and provides no information on the morphology of the outflow.

One novel way of developing these constraints is to trace the extent of winds in emission. This has been demonstrated in the optical using rest frame near infrared transitions (i.e Hα and O III etc) as tracers for nearby starbursts (Matsubayashi et al. 2009; Veilleux

et al. 2009; Tripp et al. 2011) because these transitions can trace the warm shock heated phase of the gas. However, it is difficult to use these rest frame near infrared transitions to probe winds at higher redshift because the faint emission can be redshifted into the infrared where the sky background is bright. At higher redshifts, it is advantageous to trace winds in the optical with the rest frame ultraviolet ion, Mg II (Weiner et al. 2009; Kornei et al. 2013)

Typically, studies of winds using Mg II have focused on its absorption kinematics. However, recently in a study by Rubin et al. (2011), strong Mg II emission with a P-Cygni line profile was observed in the 2D spectrum of a strongly star-forming galaxy at redshift $z = 0.694$. This emission was the first detection of an outflow beyond the spatial extent of the galaxy continuum in the distant universe, with a minimum spatial extent > 7 kpc. One proposed production mechanism for the galaxy's observed Mg II line profile is photon scattering.

In this mechanism, Mg II ions in the region of the wind closest to the observer will absorb continuum photons in the resonant transitions, λ_{2796} and λ_{2803}. Once these transitions are excited, they may only decay back to the ground state and if the optical depth of the gas is high, then the gas will resonantly trap the absorbed photons. Because the photons are absorbed in the rest frame of the gas, the absorption will be blueshifted relative to the galaxy's systematic velocity. The Mg II ions in the section of the wind farthest from the observer will absorb and scatter photons that are redshifted relative to the front portion of the wind. Because the photons are redshifted, the photons will be able to travel freely towards the observer through the wind to produce emission at and redward of the systematic velocity of the galaxy (Rubin et al. 2011). The photon scattering model, as explained, is described for the geometry of an isotropic wind (Prochaska et al. 2011). For anisotropic bi-conical winds, the emission induced from photon scattering will be highly suppressed. Since the first detection of Mg II emission by (Rubin et al. 2011), further detections of extended Mg II emission are by Erb et al. (2012) and Martin et al. (2013) have shown that emission is stronger for higher mass galaxies and that outflows can extend out to at least 18 kpc.

We aim to take advantage of this photon scattering as we present the first narrowband imaging of Mg II line emission of 5 star-forming ($z \sim 0.7$) galaxies located in the deep Great Observatories Origins Deep Survey south (GOODS-S) field. The value in using narrowband imaging is the ability to spatially resolve any absoroption and emission from a galaxy. We use two filters: a line filter and a continuum filter. The line filter covers the Mg II

doublet, while the continuum filter is off-set from line filter. The continuum filter will allow us to observe the continuum level of the galaxy near the Mg II doublet. With the resulting images taken using the two filters, we can subtract the continuum image from the Mg II image, effectively creating an image that contains only photons from Mg II. Contrary to 1D spectra, the narrowband imaging has the ability to measure the surface brightness, optical depth and radial extent of a wind. This narrowband imaging will allow us to create the first ever spatially resolved map of Mg II emission.

2. OBSERVATIONS AND DATA REDUCTION

2.1. *Sample Selection*

Our target galaxies were selected from a Keck/LRIS survey of UV absorption lines in ≈ 100 objects having redshifts $0.3 < z < 1.4$ and $B_{AB} < 23$ in fields with deep *HST*/ACS imaging (Rubin et al. 2014). In particular, this parent survey targeted galaxies in a total of nine Keck/LRIS pointings located in both of the GOODS fields (Giavalisco et al. 2004)and the AEGIS survey field (the Extended Groth Strip; Davis et al. 2007). In inspecting the redshift distribution of the portion of this sample observable from the Southern Hemisphere, we uncovered a narrow peak of nine galaxies in the interval $0.66 < z < 0.68$. This peak is in fact the global maximum of the distribution, as all other bins of width $\Delta z = 0.02$ have at most four galaxies. Moreover, there are two narrow interference filters available on VLT/FORS2 centered at $\lambda \sim 468.4$ and 472.6 nm which cover the Mg II $\lambda\lambda 2796, 2803$ transition in precisely this redshift interval. We selected our final sample of five of these galaxies at $0.66 < z < 0.68$ to be close on the sky such that they could be imaged in a single $7' \times 7'$ FORS2 pointing.

The absorption line modeling presented in (Rubin et al. 2014) indicates that these five galaxies are driving strong outflows traced by Mg II with velocities $\sim 150 - 420$ km s^{-1} and equivalent widths (EW) $\sim 2 - 3$ Å. Modeling of the galaxy broad-band spectral energy distributions obtained from multi-wavelength ancillary imaging data yields star formation rates (SFR) ranging from ~ 4 to 40 $M_\odot$ yr^{-1} and stellar masses in the range $\log M_*/M_\odot \sim 9.9 - 11.0$. The properties of the sample, as well as precise target coordinates, taken from Rubin et al. (2014) are listed in Table 2.

2.2. *VLT/FORS2 Observations*

The data were taken in service-mode using the FORS2 instrument on the VLT 8.2m telescope Antu between October 2012 and February 2013. We used two narrowband filters, HeII+47 and HeII/3000+48, that have

peak transmission at wavelengths that correspond to the Mg II doublet lines at our sample redshift of $z \approx 0.7$ (see Table 1). The transmission curves are plotted along with each galaxy's spectrum in Figure 2.

FORS2 has a pixel scale of $0.25''$ pixel^{-1} and a field of view of $7' \times 7'$. Summing the individual exposure times for each image results in a combined exposure time of 10.0 hours each for the HeII+47 and HeII/3000+48 filters. Our observations were carried out under photometric and thin cloud conditions (program ID: 090.A-0427A). The seeing (see Figure 3) ranged from 0.5 arcsec to 2.5 arcsec. The data were taken with three pointings offset by 0.25'.

2.3. *Supplemental Keck/LRIS spectra*

In addition to VLT imaging, in the present analysis we utilize galaxy spectra taken from the Rubin et al. (2014) Keck I Low Resolution Imaging Spectrometer (LRIS) program. A $0.9''$ slit width was used for all slitmasks and the median FWHM resolution for the spectra is 274 km s^{-1} at $\lambda_{\rm rest} \approx 2800$ Å and 286 km s^{-1} at $\lambda_{\rm rest} \approx 2600$ Å (see Figure 2).

2.4. *Image Reduction*

The data were reduced using custom routines written in **Python**. The images were first corrected by subtracting and removing the overscan region of the CCD. Then the images were bias-subtracted and flat-fielded using twilight flats. To improve the flat-fielding essential for detecting faint extended emission across the fields, we further correct for the illumination patterns using night-sky flats. The night-sky flats were produced by combining the unregistered science frames with an average sigma-clipping algorithm after masking out all the objects, and any bad pixels. Each individual image was cleaned of cosmic rays and bad pixels by utilizing the L.A. Cosmic algorithm. The astrometry solutions were calculated via Astrometry.net (Lang et al. 2010) with a standard deviation in the galaxy coordinates of $\sigma \approx 0.10''$. Before image stacking, we ran each frame through **SExtractor** (Bertin et al. 1996) in order to create a root mean square (RMS) map of each science image. These frames, in addition to the science images, are stacked to create a co-added RMS image.

The final stacked images for each filter is obtained using **SWarp** (Bertin et al. 1996). Each individual frame is first sky-subtracted using a background mesh size of 256 pixels which is approximately $64''$. We chose the mesh size to be large enough such that the extended emission is not mistakenly subtracted (Arrigoni Battaia et al. 2015) . The frame, after background-subtraction, is resampled onto a common astrometric solution using a *Lancosz3* interpolation kernel. The images are average-combined and weighted by the night-flat image in order to increase the signal-to-noise of any Mg II emission. **SWarp** is also configured to produce RMS weight maps from our **SExtractor** weighted images. Our final stacked images in each filter are shown in Figure 4 with the target galaxies indicated.

One side effect from stacking is that the east and west borders of each image contain greater noise compared to the center of the image. This is due to the imperfect overlap of the 3 pointings used. However, the sample galaxies are sufficiently distant from these low S/N regions that their photometry is not affected.

Table 1. VLT/FORS2 Observations: Filter and exposure properties of the VLT observations. The width of the transmission curves are calculated by convolving the transmission curve with the total wavelength range of the filter. These values differ slightly from those reported by the European Space Observatory.

Filter	λ_{eff}(Å)[a]	λ_{width}(Å)	$N_{\rm img}$	$t_{tot}(s)$	S[b]
HeII	4675.21	50.11	38	35,959	2.45
HeII/3000	4722.46	44.82	38	36,937	2.40

[a] λ_{eff} is the effective wavelength of the filter transmission curve.
[b] S is in units of 10^{-17} ergs counts^{-1} cm^{-2}

2.5. *Absolute Flux Calibration*

We acquired observations of the standard star GD50 from archival ESO calibration imaging at 4 independent epochs. From this standard we calculated the atmospheric extinction coefficients to be 0.181 magnitudes for the HeII/3000+48 filter and 0.190 magnitudes for the HeII+47 filter. Since we have imaging of the standard star GD50 in our two filters, and access to GD50's spectral energy distribution (cite!) and each filter's transmission curve through the ESO website, we are able to perform absolute flux calibration using the methods of Jacoby et al. (1990). We first convolve the spectral energy distribution of the standard star, $F(\lambda)$ in ergs sec^{-1} Å^{-1} cm^{-2}, with that of the known transmission curve of the filter, $T_i(\lambda)$. This yields F_i, the total observable flux in each bandpass filter i with units of ergs sec^{-1} cm^{-2}:

$$F_i = \int F(\lambda)T_i(\lambda)d\lambda.$$

It is not uncommon to assume that $F(\lambda)$ is constant over the small width of the filter. However, our filter transmission curves are sampled at 5 Å intervals which is the same sampling as the spectral energy distribution of the standard star obtained from the ESO archives. Therefore we calculate the integral numerically. The
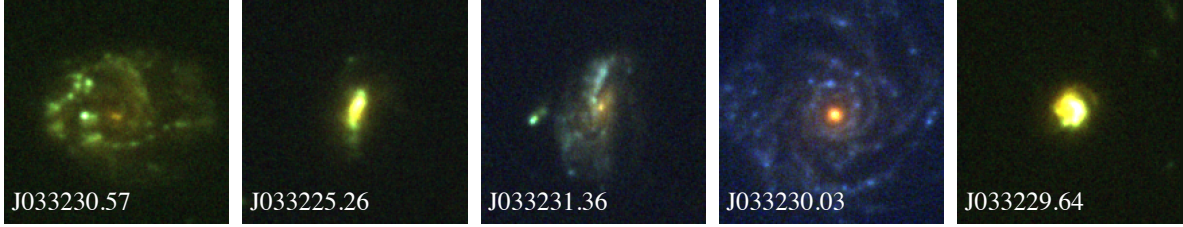
Figure 1. Color imaging of our sample galaxies in the *HST*/ACS F435W, F606W, and F775W filters obtained as part of the GOODS survey (Giavalisco et al. 2004). Each image is 5" × 5".

Table 2. Properties of 5 galaxies in our sample : All galaxies are at roughly the same redshift. The star formation rates for the sample range from 3.8 to 40.5 solar mass per year. The EW include both components of the Mg II doublet and were calculated with Eq. 6 and the supplemental Keck/LRIS spectra. *HST*/ACS images of the galaxy sample are shown in Figure 1. The Keck/LRIS spectroscopy of this sample published in Rubin et al. (2014) is shown in Figure 2

Object	R.A.	Dec	z	SFR($M_\odot$ yr^{-1})	log $M_*/M_\odot$	EW(Å)
J033225.26-274524.0	03:32:25.26	-27:45:23.9	0.6660	$9.1^{+1.3}_{-3.7}$	$9.86^{+0.05}_{-0.04}$	7.539 ± 0.354
J033231.36-274725.0	03:32:31.35	-27:47:24.9	0.6669	$10.5^{+1.7}_{-1.6}$	$10.02^{+0.03}_{-0.03}$	5.835 ± 0.493
J033230.03-274347.3	03:32:30.03	-27:43:47.2	0.6679	3.8^{+0}_{-0}	$10.98^{+0.01}_{-0.0}$	12.794 ± 1.710
J033229.64-274242.6	03:32:29.64	-27:42:42.5	0.6671	$40.5^{+8.2}_{-12.1}$	$10.30^{+0.07}_{-0.03}$	13.239 ± 0.263
J033230.57-274518.2	03:32:30.56	-27:45:18.2	0.6807	$12.6^{+1.7}_{-2.1}$	$10.48^{+0.03}_{-0.07}$	6.106 ± 0.370

system sensitivity, including the defects of the telescope optics and detector response is then given by

$$S_i = \frac{F_i}{C 10^{k_i A}},$$

where k_i is the extinction in magnitudes per airmass, A is the airmass for each individual exposure, C is the measured count rate of the standard star and S is in units of ergs counts^{-1} cm^{-2}. Before image co-addition, each science image is corrected for atmospheric extinction by multiplying each frame by $10^{k_i A}$. Next, the image is divided by the exposure time, effectively putting the image in units of counts per sec. After co-addition, the images are then multiplied by the appropriate sensitivity factor S_i. This puts the final images in the appropriate flux units ergs sec $^{-1}$ cm^{-2}.

3. ANALYSIS

We have two goals for our study: (1) assess the surface brightness of line emission in the Mg II transition in and around each target galaxy; and (2) spatially resolve the morphology of the strong Mg II absorption observed against the galaxy continua. To reach the both of these goals, we must perform accurate subtraction of the continuum flux of each object from the filter covering the targeted line emission. For four of the five objects in our sample, the HeII+47 image includes both line and continuum emission, and the HeII3000+48 image provides a high S/N measurement of the continuum only ≈ 30 Å redward of the line emission in the rest-frame. We detail our method of continuum subtraction using these data in Section 3.2 below, and follow with a presentation of the resulting surface brightness profiles (Section 3.3) and EW images (Section 3.4).

3.1. *Spectral Correction*

With the supplementary spectra from (Rubin et al. 2014), we can fit the continuum and determine the slope of each galaxy spectrum in order to test whether the spectral slope gives rise to differences in continuum flux between the two filters. We use the interactive fitting routine **lt_continuumfit** from the linetools package
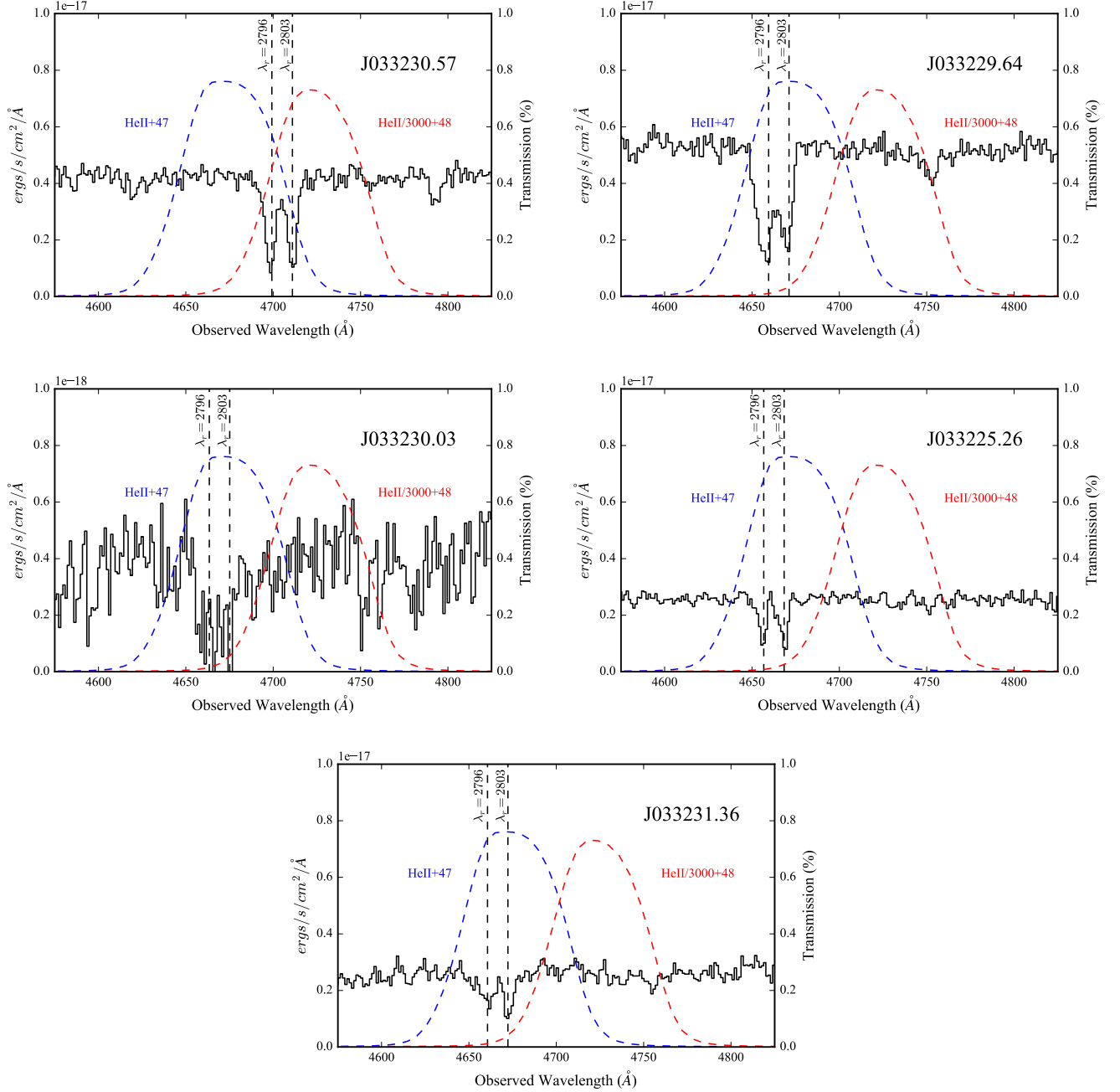
Figure 2. KECK/LRIS spectrum of the sample galaxies and the transmission curves of the filters HeII+47 and HeII/3000+48. The left-hand axis is in units of flux density and the right-hand axis is the percentage of light transmitted the filter at each wavelength. Vertical dotted lines indicate the wavelength of the redshifted Mg II doublet. The Mg II doublet falls fortuitously at the central wavelength of the HEII+47 filter.

(Prochaska et al. 2016)[1] to fit the continuum. By fitting the continuum we are masking the absorption features and making an effectively flat spectrum, which we use as a model. We find the total flux in each filter by convolving the fitted continuum with each filter's transmission curve. Next, we take the ratio of both integrated totals, as the ratio will indicate the scaling factor needed to correct our flux measurements prior to continuum subtraction. Comparing these ratios between each galaxy, we find that each ratio is effectively the same, within 3 decimal places, with a value of 1.118. This value is equal to the ratio between the FWHM of the transmis-
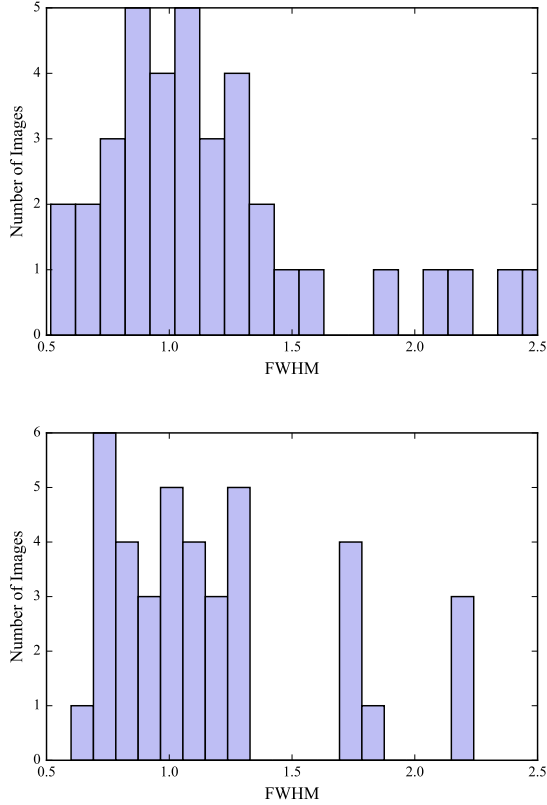
[1] https://github.com/linetools/linetools

Figure 3. Distribution of seeing conditions for individual exposures comprising our dataset. **Top**: Seeing distribution for the 38 HeII+47 images. The median seeing in this filter is $1.03''$. **Bottom**: Same distribution for the 38 HEII/3000+48 images. The median seeing is $1.08''$. The seeing conditions were calculated by ESO and were provided in the header of each science image.

sion curves, allowing us to conclude that the slope of the spectrum of each galaxy is flat, and hence that the continuum level measured in the off-line filter provides an accurate measure of the continuum contribution to the on-line filter flux.

3.2. *Continuum Subtraction*

To properly continuum-subtract the image taken with the emission filter in excess of the continuum, we follow a prescription given by Arrigoni Battaia et al. (2015). We first determine the continuum flux density from the off-Mg II filter,

$$f_{cont} = \frac{F_{cont}}{\Delta\lambda_{cont}}, \tag{1}$$

where F_{cont} and $\Delta\lambda_{cont}$ are the observed flux per pixel of the continuum image per pixel and the transmission FWHM of the continuum filter, respectively. With f_{cont}

it is then possible to calculate the flux of any excess emission, F_{line}:

$$F_{line} = F_{MgII} - f_{cont}\Delta\lambda_{MgII} \tag{2}$$

where F_{MgII} and $\Delta\lambda_{MgII}$ are the observed flux per pixel in the Mg II filter and the transmission FWHM of the Mg II filter. The continuum subtracted images of each galaxy are shown in Fig. 5.

3.3. *Surface Brightness Profiles and Limits*

In order to test for the presence of Mg II emission, we perform aperture photometry on the continuum subtracted images using the python library Photutils. We choose annuli with a radial thickness of 1 pixel or $0.25''$, such that, $r_{inner} = r_{outer} - 1$ (in pixels). Each annulus is centered on the flux-weighted centroid of the galaxy. By dividing the summed flux in each annulus by the area in arcseconds we produced surface brightness (SB) profiles for each galaxy which are shown in Figure 9.

The error in this quantity is determined from an RMS image produced by **SWarp**. We place annuli that are identical to the annuli used to find the SB profiles for each galaxy. To calculate the variance inside each annulus, we sum the RMS pixel values in quadrature, then divide by the area of each annulus.

To calculate the 1σ SB limit we follow the recipe found in Arrigoni Battaia et al. (2015). We first masked out all the sources, their associated extended halos, and edge noise in both the HEII+47 and HEII/3000+48 images. We then calculate the root-mean-square (rms) of the background in randomly placed 1" apertures. We convert these rms values to SB limits *per* 1 sq.arcsec aperture. We find that the 1σ detection limits per 1 arcsec^2 aperture (SB_1) are 6.332×10^{-19} ergs sec^{-1} cm^{-2} arcsec^2 and 5.808×10^{-19} ergs sec^{-1} cm^{-2} arcsec^2 in the HeII/3000 and HeII filters, respectively. With the 1σ detection limit, SB_1, determined for the continuum+Mg II (HeII) image, we define an extended annulus to be used to detect any extended Mg II emission. This extended annulus has an inner radius approximately the size of a unique SB_1 isophotal contour for each galaxy. The outer radius will be the inner radius extended by an arbitrary choice of 5 pixels.

The sensitivity required to detect an extended source depends on its size because one can reach lower SB levels by spatially averaging over large apertures. In the ideal case of perfect sky subtraction and continuum subtraction, the 1σ SB limit for an extended source is $SB_1/\sqrt{A_{\mathrm{src}}}$, where A_{src} is the area in arcsec^2 and SB_1 is the surface brightness limit per 1 arcsec^2 aperture. In practice, the actual detection limits are limited by systematics from imperfect subtraction. Therefore, we empirically determine the limits as follows. We mask all the
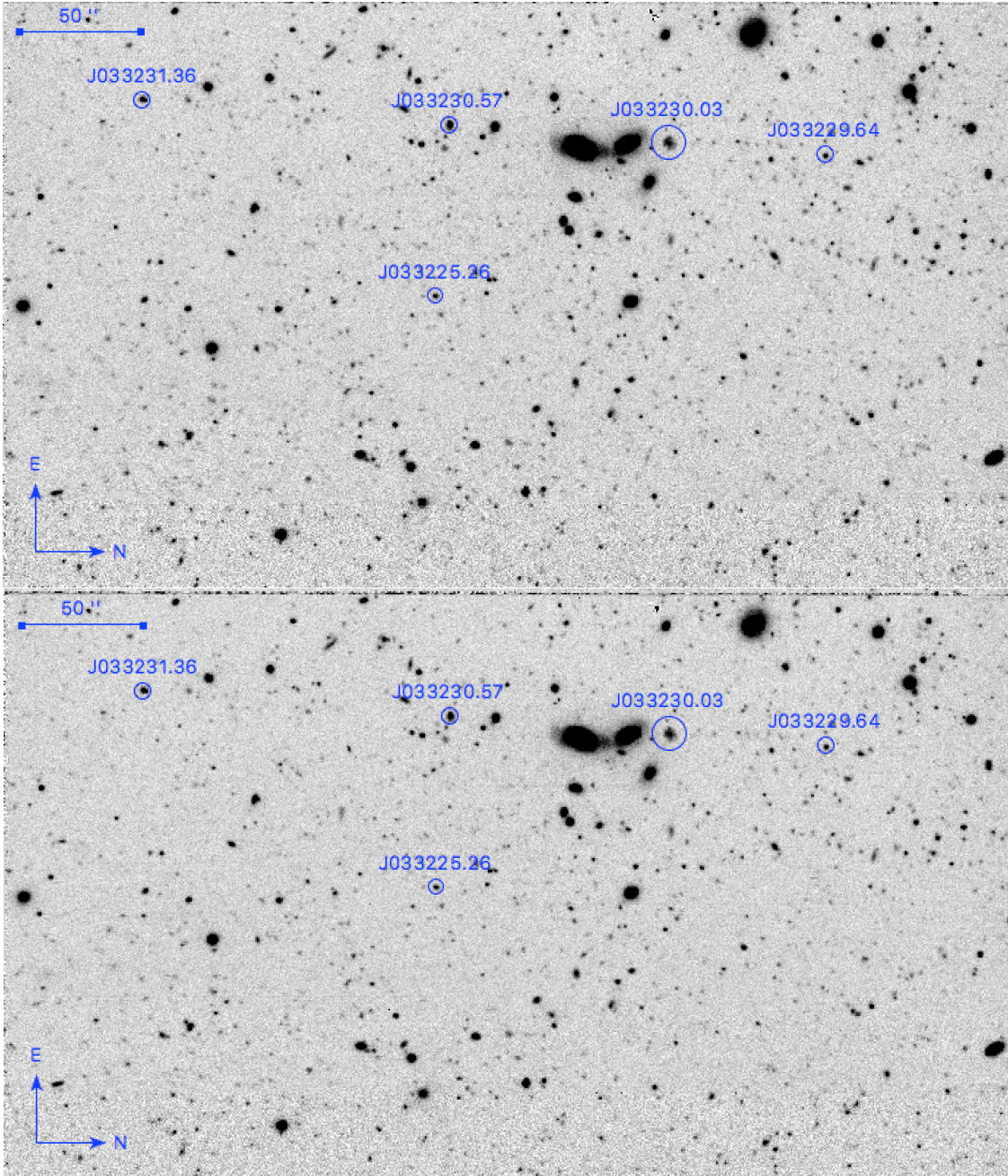
Figure 4. Top: HeII+47 image after stacking. Bottom: HeII3000+48 image after stacking. The exposure time of each image is ≈ 10 hours. Each image has a FOV of $7' \times 7'$ which fortuitously contains the full sample of galaxies (indicated by the blue circles) in a single pointing. East is up and North is right.

artifacts and sources in the continuum-subtracted images. Next generate randomly sized annuli, place them at random and extract the fluxes, $F_{\rm src}$, within these annuli. In the ideal case that the sky and continuum are perfectly subtracted, the fluxes, $F_{\rm src}$, from many random annuli should follow a Gaussian distribution with a width of $\sigma_{\rm src} \equiv SB_1\sqrt{A_{\rm src}}$. We find that the actual Gaussian width, $\sigma'_{\rm src}$ of the distribution is broader than

$\sigma_{\rm src}$. We adopt $F_{\rm limit} \equiv \sigma'_{\rm src}$ as the 1σ upper limit on the total line flux of extended Mg II emission.

In order to show that our detection limits are reasonable, we create simulated emission with varying intensities to see if we can visually detect any Mg II emission. The results of this exercise are shown in Figure 7 For each galaxy, we assume a constant surface brightness corresponding to an excess of surface brightness 0, 1, 3, 5, 10 and 20 times the 1σ $SB_{\rm limit}$ inside the largest annu-
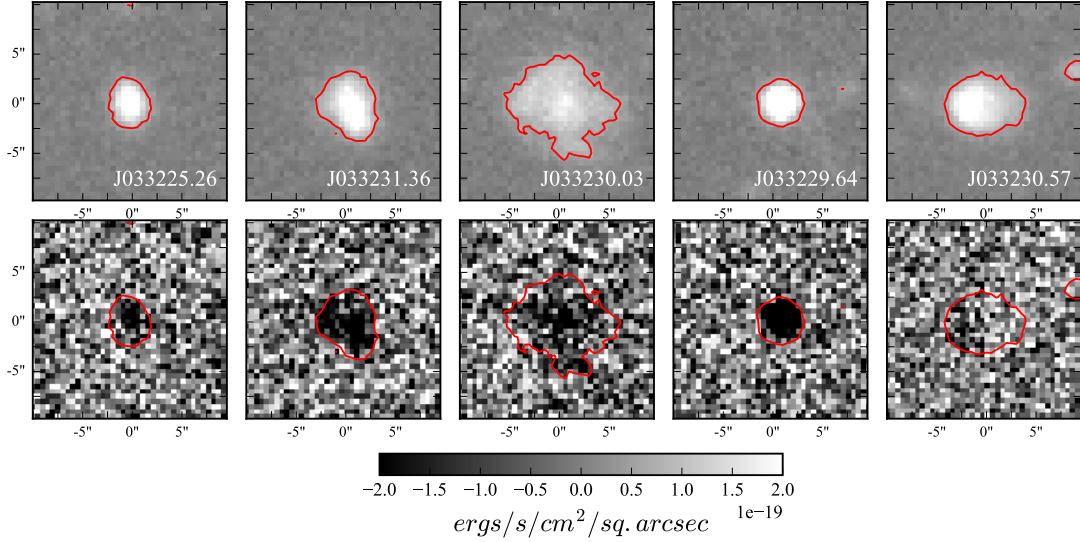
Figure 5. $10'' \times 10''$ images of each galaxy in our sample. Top row: Continuum flux in ergs/s/cm^2/sq.arcsec. Bottom row: Continuum subtracted Mg II flux. Absorption can be seen in 4 of 5 galaxies. The red contours represent the outline of the 1σ surface brightness limit of continuum flux in the HeII/3000+38 image, defined in Sec. 3.3. The colorbar shows the scaling used for the line emission images.
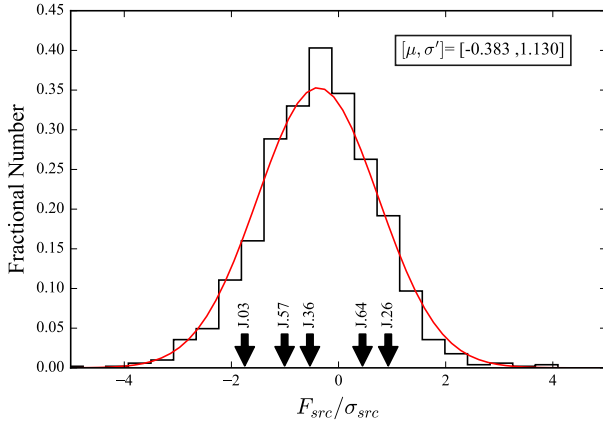

Figure 6. Normalized distribution of F_{src}/σ_{src} values, for random circular annuli. F_{src} is the total flux within the largest annulus and σ_{src} is the expected 1σ flux limit in the ideal case of perfect sky and continuum subtraction, i.e $SB_1\sqrt{A_{src}}$.

lus used. Additionally, we assume gaussian noise with a variance equal to $1SB_{limit}$. After placing the simulated emission around the galaxy, we subtract the continuum in the same manner as explained in Section 3.2. To test the detectability of measuring extended emission we construct a smoothed χ image following the technique in Hennawi & Prochaska (2013) and Arrigoni Battaia et al. (2015). First, we smooth the continuum-subtracted image:

$$I_{smth} = \text{CONVOLVE[NB-CONTINUUM]}, \quad (3)$$

Table 3. Significance of Extracted Flux

Object	F(Mg II)[a]	Area[b]
J033225.26-274524.0	2.44(0.92)	21
J033232.36-274725.0	-1.40(-0.53)	21
J033230.03-274347.3	-5.23(-1.75)	27
J033229.64-274242.5	1.23 (0.44)	26
J033230.57-274518.2	-2.53 (-1.00)	18

[a]Mg II flux is in 10^{-18} ergs sec^{-1} cm^{-2}. The value in the parenthesis is the statistical significance with respect to σ_{src}
[b]Area of the extended annulus in sq.arcsec

where the CONVOLVE operation indicates convolution of the images with a Gaussian kernel with FWHM=1.5 pixels. Next, we computed the sigma image (σ_{smth}) for the smoothed image (I_{smth}) by propagating the noise image of the unsmoothed data:

$$\sigma_{smth} = \sqrt{\text{CONVOLVE}^2[\sigma^2_{unsmth}]}, \quad (4)$$

where the CONVOLVE^2 operation indicates the convolution of the noise image with the square of the Gaussian kernel. The smoothed χ image is defined by

$$\chi_{smth} = \frac{I_{smth}}{\sigma_{smth}}. \quad (5)$$

This χ_{smth} image aids in recognizing the presence of extended Mg II emission.

Figure 7 shows the χ_{smth} image for the synthetic Mg II emission. Galaxies are outlined by a black isophotal contour corresponding to $1SB_1$ and the simulated emission

Table 4. Empirically Determined Detection Limits

Object	5SB$_{\mathrm{limit}}$[a]	Area[b]
J033225.26-274524.0	6.51	21
J033232.36-274725.0	6.51	21
J033230.03-274347.3	5.74	27
J033229.64-274242.5	6.22	26
J033230.57-274518.2	6.81	18

[a]Limits are in 10^{-19} ergs sec $^{-1}$ cm^{-2} arcsec^2

[b]Area of the extended annulus in sq.arcsec

is contained inside an annulus surrounding the contours. The χ_{smth} images confirm that we should be able to detect extended Mg II emission down to a conservative level of 5SB$_{\mathrm{limit}}$. Note again that the SB$_{\mathrm{limit}}$ does indeed take into account the systematics from imperfect continuum subtraction.

3.4. *Equivalent Widths*

Here we derive an expression to calculate the equivalent width (EW) of any absorption or emission features observed in our narrow-band imaging. Starting from the expression for EW used in the context of spectroscopy,

$$EW = \int (1 - \frac{f_{line}}{f_{cont}})d\lambda \tag{6}$$

we begin by dividing Eq 2 by the flux density of the continuum and the FWHM of the on-line filter,

$$\frac{F_{line}}{f_{cont}\Delta\lambda_{MgII}} = \frac{F_{MgII}}{f_{cont}\Delta\lambda_{MgII}} - 1. \tag{7}$$

Next, we rearrange the above expression such that we produce the argument of the integrand in Eq. 6 on the RHS,

$$-\frac{F_{line}}{f_{cont}\Delta\lambda_{MgII}} = 1 - \frac{f_{MgII}}{f_{cont}}. \tag{8}$$

We then approximate the integration in Eq. 6 by multiplying the integrand above by the FWHM of the on-line filter $d\lambda = \Delta\lambda_{MgII}$,

$$-\frac{F_{line}}{f_{cont}} = (1 - \frac{f_{MgII}}{f_{cont}})\Delta\lambda_{MgII}; \tag{9}$$

such that

$$EW = -\frac{F_{line}}{f_{cont}}. \tag{10}$$

Using the above equation along with the continuum and continuum-subtracted images, we produce images of the EWs. The EW images are displayed in Figures 10, 11, 12, 13, 14, and show only the EWs within the 1σ SB$_1$ contours of the corresponding Mg II images (prior to continuum subtraction).

To compare our map of EWs to the values measured from the Keck/LRIS spectra, we place 0.9 arcsec wide apertures on top of each galaxy. The width and angle of the apertures replicate the orientation of the slits used to obtain the spectra. Next, we determine which pixels lie outside the 1σ SB$_1$ contours and set those to zero. Outside this contour, the EWs become poorly constrained due to the lack of S/N in the continuum. We then apply a S/N = 1.5 cut to the continuum image and create a histogram to show the distribution of EWs as shown in Figures 4.5 through 4.5. Having removed EWs with low-S/N continuum values from our images, we compute the mean equivalent width inside the Keck/LRIS apertures. These values are summarized in Table 5.

In order to get information on the morphology of the Mg II, we determine the distance of each pixel from the center of each galaxy in kiloparsecs. We plot the EWs over this projected distance for each galaxy in Figures 4.5 through 14. Although some of the plots suggest a slight upward trend in the values of the EW at increasingly large radii, we cannot be confident in this trend because of large scatter. To better visualize the data and test the significance of the trend, we bin the data radially. For example, in Figure 13, the EW from absorption extends out to ~ 25 kpc. The EWs are binned in 5 kpc increments. We calculate the mean and scatter of the EWs in each bin and show these values in Figure 15.

4. DISCUSSION

In this chapter we present the results from the continuum-subtraction of the off-line continuum filter to that of the on-line emission filter.

4.1. *Limits on MgII emission*

We do not detect any significant amount of Mg II emission in any of our sampled galaxies. The χ_{smth} images shown in Figure 7 confirm this. A comparison of the simulated emission with the χ_{smth} image of the original stamps, shown in the first column, similarly suggests that we do not detect any extended Mg II emission. We thus place conservative 5σ upper limits on Mg II emission for each galaxy in the sample, summarized in Table 4. The most sensitive detection limit using the largest area is SB(Mg II) = 5.74×10^{-19} ergs sec $^{-1}$ cm^{-2} arcsec^2, computed for the galaxy J033230.03. Our least sensitive detection limit is SB(Mg II) = 6.81×10^{-19} ergs sec $^{-1}$ cm^{-2} arcsec^2, computed for the galaxy J033230.57.

4.2. *Previous Detections of extended Mg II emission*

Previous constraints on the brightness of scattered Mg II emission were reported by Rubin et al. (2011).
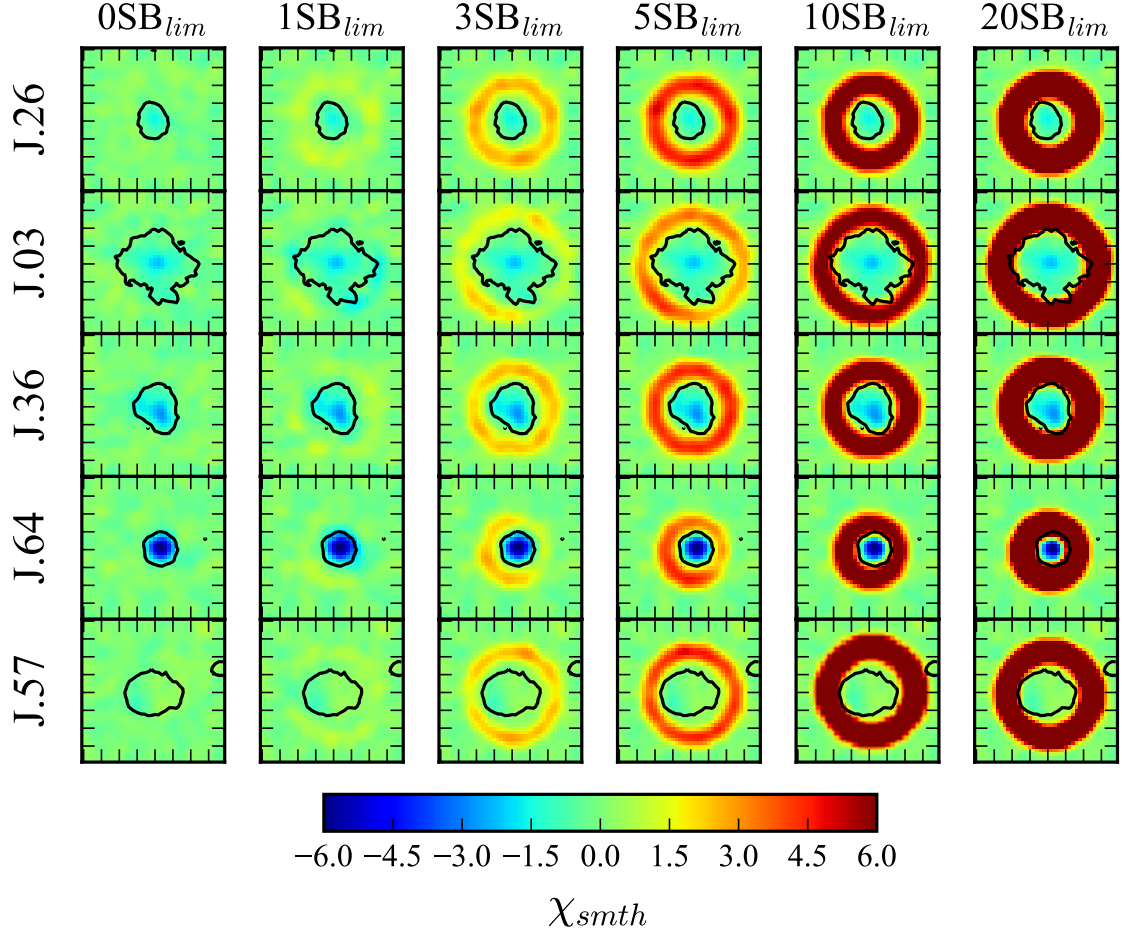
Figure 7. Postage stamp χ_{smth} images of the 5 galaxies in our sample. Every galaxy is placed in the same row in each column. The columns show simulated emission, with levels of 0, 1, 3, 5, 10, and 20 times SB_{lim}. Each postage stamp has a size of $5'' \times 5''$ (corresponding to 35 kpc $\times$ 35 kpc at $z \sim 0.70$). Each stamp shows the galaxy along with the same isophotal contour used in previous figures. Comparing the $0\mathrm{SB}_{\mathrm{limit}}$ column with the continuum-subtracted images in Figure 5 suggests that we did not detect any Mg II emission.

In this work the authors studied emission from the starburst galaxy TKRS 4389 at $z = 0.69$ with a star formation rate of 49.8 $M_\odot$ yr^{-1}. This emission was detected in a 2-dimensional KECK/LRIS spectrum, with flux from the emission reaching 8.0 ± 0.4 and 4.4 ± 0.4 $\times 10^{-18}$ ergs sec^{-1} cm^{-2} at λ_{2796} and 4.0 ± 0.3 and 2.5 ± 0.4 $\times 10^{-18}$ ergs sec^{-1} cm^{-2} at λ_{2803} in two independent locations spatially offset from the galaxy continuum. The flux from the emission can be converted into two surface brightness values by taking the average of the flux measured at each location and each transition, and dividing by a 1 sq.arcsec aperture.

Figure 8 shows a plot of the 5σ detection limits determined for each galaxy in our sample as well as the SB calculated for the galaxy TKRS 4389. The figure suggests that we should be able to detect scattered Mg II emission with strengths similar to that detected in TKRS 4389. Given if additional detections of extended Mg II emission are made, it could be possible that there exists the possibility of a relationship between SB and star-formation rate, as the study by Erb et al. (2012) discuss that emission strength is stronger in high mass galaxies. This could be one explanation as to why we did not detect any extended Mg II emission Further studies need to be pursued to add additional points to Figure 8.
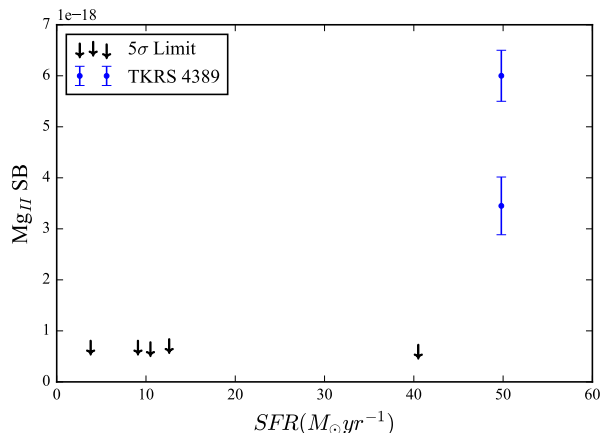

Figure 8. Comparison of our detection limits to the measured extended emission of TKRS 4389. Our imaging is sufficiently sensitive to detect extended emission at similar strengths to the extended emission measured for TKRS 4389.

4.3. *Geometry of re-emitted photons*

In idealized wind models of cool gas outflows, discussed in Prochaska et al. (2011), strong Mg II emission is predicted to be generated along with ubiquitous blueshifted absorption of Mg II. For isotropic and dust-free scenarios, this absorption and emission is simply produced by the conservation of photons, as any absorbed continuum photon is eventually re-emitted in emission. Because of this photon exchange the total equivalent width of both the absorption and emission features is equal to zero. Assuming that our galaxies host an isotropic and dust-free wind, we wish to determine how much emission is predicted to be missing from our imaging, and how the SB of this missing emission compares to our detection limits, for different distributions of emission.

To find the amount of missing emission, we first calculate how much continuum has been absorbed by Mg II. Using our Keck/LRIS spectra, we find the average value of the continuum near the Mg II doublet and multiply this value by the EW of the doublet. Although we know how much emission is missing, we do not know how this emission is distributed outside the galaxy. As a conservative estimate of the SB, we distribute the missing emission uniformly inside multiple and increasingly sized annuli. These annuli are fixed to have an inner radius equal to the galaxy's isophotal radius and an increasing outer radius. Additionally, since our SB limits are dependent on the size of the aperture used, we calculate the SB detection limits of our images inside each of the aforementioned annuli. Figure 16 shows how the SB of emission varies with the spatial extent of the annulus, as well as how the SB compares with our detection limits. Excluding the galaxy J033230.03, the SB of this missing emission lie above our detection limits. This result shows that these galaxies do not host an isotropic dust-free wind.

There are many phenomena that we can employ to reduce the SB of the missing Mg II emission to better match our observations. Introducing dust into the wind can reduce the observed emission as it can change the observed line profile in a critical way as re-emitted photons have to travel farther distances to escape the wind and therefore the profile will suffer greater extinction. Another factor that can reduce the amount of emission is anisotropy of the wind. Isotropic winds are idealized, but galaxies are not spherically symmetric and the shape of the galaxies interstellar medium may preferentially suppress outflows at varying strengths for different galactic longitudes. We now assume that the emission in our galaxies is reduced by purely by the effects anisotropy, as the constraints on dust attenuation or unknown. For the anisotropic winds modeled in Prochaska et al. (2011), the factor that the emission is reduced is given by the scaling $\Omega/4\pi$, where Ω is the angular extent of the wind which is constrained to point towards the observer $\Omega > 2\pi$. We show the anisotropic wind SB profiles in Figure 16.

After reducing the SB of the missing Mg II emission by the minimum opening angle $\Omega = 2\pi$, we are able to profiles that fall below our SB detection limits for galaxy's J033225.26 and J033231.36. However, the SB profile of J033229.64 remains above our SB detection limits, suggesting additional phenomena are needed to reduce the strength of missing emission.

4.4. *Spatially Resolved Maps of Mg II Absorption*

In this section we discuss the details of the absorption detected in our images and compare our measurements to those obtained in the Keck/LRIS spectra of each galaxy..

4.4.1. *Mg II absorption in surface brightness profiles*

Although we do not detect any extended Mg II emission, we do observe a decrement of flux in the SB profiles of 4 out of 5 galaxies in our sample.

4.4.2. *J033225.26*

Figure 9 shows the SB profile for J033225.26. We report that the maximum decrement in the SB profile due to absorption is strongest at the center of the galaxy. The SB measured in the center aperture is -5.39 $\pm$ 0.128 $\times 10^{-18}$ erg s^{-1} cm^{-2} per sq.arcsec. The absorption in the profile decreases radially outward and is detected out to the largest distance sampled, $\sim$ 18 kpc, away from the center of the galaxy.

4.4.3. *J033231.36*

Figure 9 shows the SB profile for J033231.36. We report that the maximum decrement in the SB profile due to absorption is strongest at the center of the galaxy. The SB measured in the center aperture is -5.64 $\pm$ 0.121 $\times 10^{-18}$ erg s^{-1} cm^{-2} per sq.arcsec. The absorption in the profile decreases radially outward and is detected out to the largest distance sampled, $\sim$ 18 kpc, away from the center of the galaxy.

4.4.4. *J033230.03*

Figure 9 shows the SB profile for J033230.03. We report that the maximum decrement in the SB profile due to absorption is strongest at the center of the galaxy. The SB measured in the center aperture is -4.41 $\pm$ 0.622 10^{-18} erg s^{-1} cm^{-2} per sq.arcsec. The absorption in the profile decreases radially outward and out to the largest distance sampled, $\sim$ 25 kpc, away from the center of the galaxy.

4.4.5. *J033229.64*

Figure 9 shows the SB profile for J033229.64. We report that the maximum decrement in the SB profile due to absorption is strongest at the center of the galaxy. The SB measured in the center aperture is -18.2 $\pm$ 0.127 $\times 10^{-18}$ erg s^{-1} cm^{-2} per sq.arcsec. The absorption in the profile decreases radially outward and is detected out to the largest distance sampled, $\sim$ 14 kpc, away from the center of the galaxy.

4.4.6. *J033230.57*

Figure 9 shows the SB profile for J033230.57. The absorption decrement is strongest at the center of the galaxy with a SB value of -1.25 $\pm$ 1.15 10^{-18} erg s^{-1} cm^{-2} per sq.arcsec. However, the measured SB of this decrement including error is consistent with measuring zero absorption. The measurement of zero absorption for J033230.57 was expected. Figure 2 shows the KECK/LRIS spectrum of J033230.57 and the transmission curves of the filters HeII+47 and HeII/3000+48. The Mg II transitions of the galaxy are equally sampled by both of our filters. Simply put, each image of J033230.57 contains equal amounts of continuum and Mg II. When we subtract the continuum image from the Mg II image we are effectively canceling out the Mg II absorption as well. This measurement can stand as a test of the quality of our continuum subtraction.

The surface brightness profiles presented in Figures 9 do not exhibit any signs of extended Mg II emission.

4.5. *Morphology of MgII Absorption*

Figures 4.5 through 4.5 show the EW images, distributions and radial projections of Mg II EWs. We have zeroed out any EWs that lie outside the SB$_1$ contours for each galaxy. We imposed a signal-to-noise cut, only including EWs where the continuum flux S/N greater than |1.5|. The mean EW is computed for all pixels inside each Keck/LRIS aperture, defined in Sec. 3.4, and are summarized in Table 5. Comparing our measured EWs with those measured from the spectra, we find good agreement to within 1σ or 2σ for most of the galaxies except and J033230.57.

In the case of J033230.57 we can easily understand why the EW measured is not in agreement with the spectra EW. Figure 9 shows the SB profile coverage of J033230.57, in this galaxy's profile we do not detect any significant decrements due to absorption. This is due to the fact that our two filters cover the Mg II doublet equally, see Figure 2. Any signal of absorption in the EW images arise from noise. Figure 4.5 shows the radial projection of the EWs measure for this galaxy which are centered around zero.

To get a better sense of how the EW of Mg II absorption changes with radius as well as account for any

Table 5. Properties of Mg II Absorption

Object	Max(SB$_{abs}$)[a]	$R_{SB_1}(kpc)$	EW(Å)[b]	EW(Å)[c]
J033225.26-274524.0	-5.39 ± 1.28	8	3.511 ± 0.795	7.539 ± 0.354
J033232.36-274725.0	-5.64 ± 0.121	15	7.694 ± 1.016	5.835 ± 0.493
J033230.03-274347.3	-4.41 ± 0.622	21	5.388 ± 0.712	12.79 ± 1.710
J033229.64-274242.5	-18.2 ± 0.127	10	7.546 ± 0.660	13.24 ± 0.263
J033230.57-274518.2	-1.25 ± 1.15	11	-0.6532 ± 0.589	6.106 ± 0.370

[a]SB Values are in units of 10^{-18} ergs sec^{-1} cm^{-2} arcsec^2

[b] Measured from EW images

[c]Measured from Keck/LRIS spectra

effects due to seeing, $\sim 7kpc$, we bin the EWs in radial bins with 5, 4 or 3 kpc widths as shown in Figures through . A majority of the galaxies appear to show large scatter in the EWs out to larger radii. To better understand the significance of these trends, we construct a plot that compiles the mean EWs for all the galaxies, shown in Figure 15. To take into account the varying size of the galaxies, we normalize the distances by the approximate radius of the SB$_1$ contour for each galaxy.

Upon inspection of Figure 15, we see that all the galaxies exhibit a constant mean EW inside our 1SB$_1$ isophotal radius.

5. CONCLUSION

We presented the results from a narrowband imaging search for Mg II emission in a sample of star-forming galaxies at a redshift of $z \sim 0.70$. Although we were unable to detect any measurable amount of Mg II emission, we are able to report a conservative 5σ detection limit of SB(Mg II) = 5.74 $\times10^{-19}$ ergs sec^{-1} cm^{-2} arcsec^2. We detected a significant amount of Mg II absorption in a total of 4 galaxies out of our 5 galaxy sample. Furthermore, our imaging allows us to generate spatially-resolved maps of Mg II absorption in a distant galaxy sample for the first time. This absorption covered the center of the galaxies out to the SB$_1$ continuum + Mg II isophotal radius, at approximately ~ 22 kpc, suggesting that the absorbing gas fully covers the stellar disks out to this distance. The measured EWs measured in these maps are in broad agreement with measured EWs using Keck/LRIS integrated slit spectroscopy. Additionally, our radial projections of the mean EW for our sample galaxies suggest that the EWs due to Mg II are approximately constant out towards the edges of the galaxies.

Finally, we compared our detection limits with estimated SB Mg II emission, based on the radiative transfer models of Prochaska et al. (2011). We are able to rule out that the winds in our sample are isotropic, as our detection limits are suitable to detect the predicted emission. By assuming anisotropic winds, we were able to reduce the strength of the predicted emission to lie below our detection limit, albeit one galaxy that needs additional phenomena like dust to achieve non-detectability in our images.

Based on the radial extent and strength of our measured Mg II absorption, the Mg II is optically thick. Deeper images in Mg II are required to observe any extended emission beyond the depth of our images. Although we are able to rule out that the winds in our sample are isotropic and dust-free, questions linger on weather the wind is anisotropic as well as dust-free. A new generation of instruments such as the Keck Cosmic Web Imager (KCWI) or the Multi Unit Spectroscopic Explorer (MUSE) should be used to answer the prevailing questions
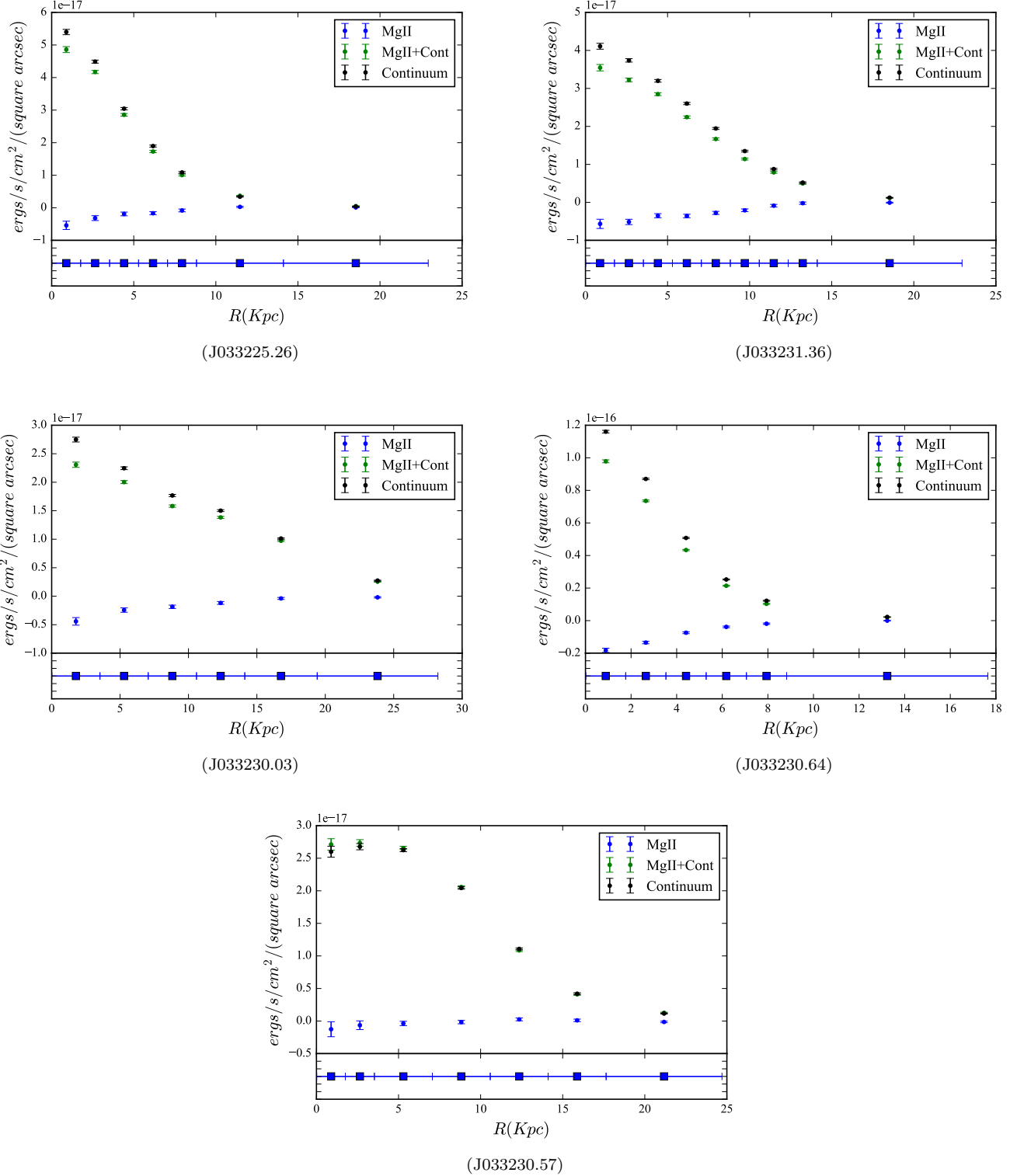
(J033225.26)

(J033231.36)

(J033230.03)

(J033230.64)

(J033230.57)

Figure 9. SB profile for our sample galaxies. (Top) Continuum SB (black) measured for the galaxy in the continuum image. Mg II + continuum SB (green) measured for the galaxy in the pre-continuum subtracted image. Mg II line SB (blue) measured for the galaxy in the continuum subtracted line emission image.The profile exhibits SB decrements from Mg II absorption. Photometry was performed in circular annuli. (Bottom) The vertical hashes in the bottom show the inner and outer radius of each annulus in kpc. Distance from the center of the galaxy (x-axis) is computed using the average value of each annulus inner and outer radii of each annuli.
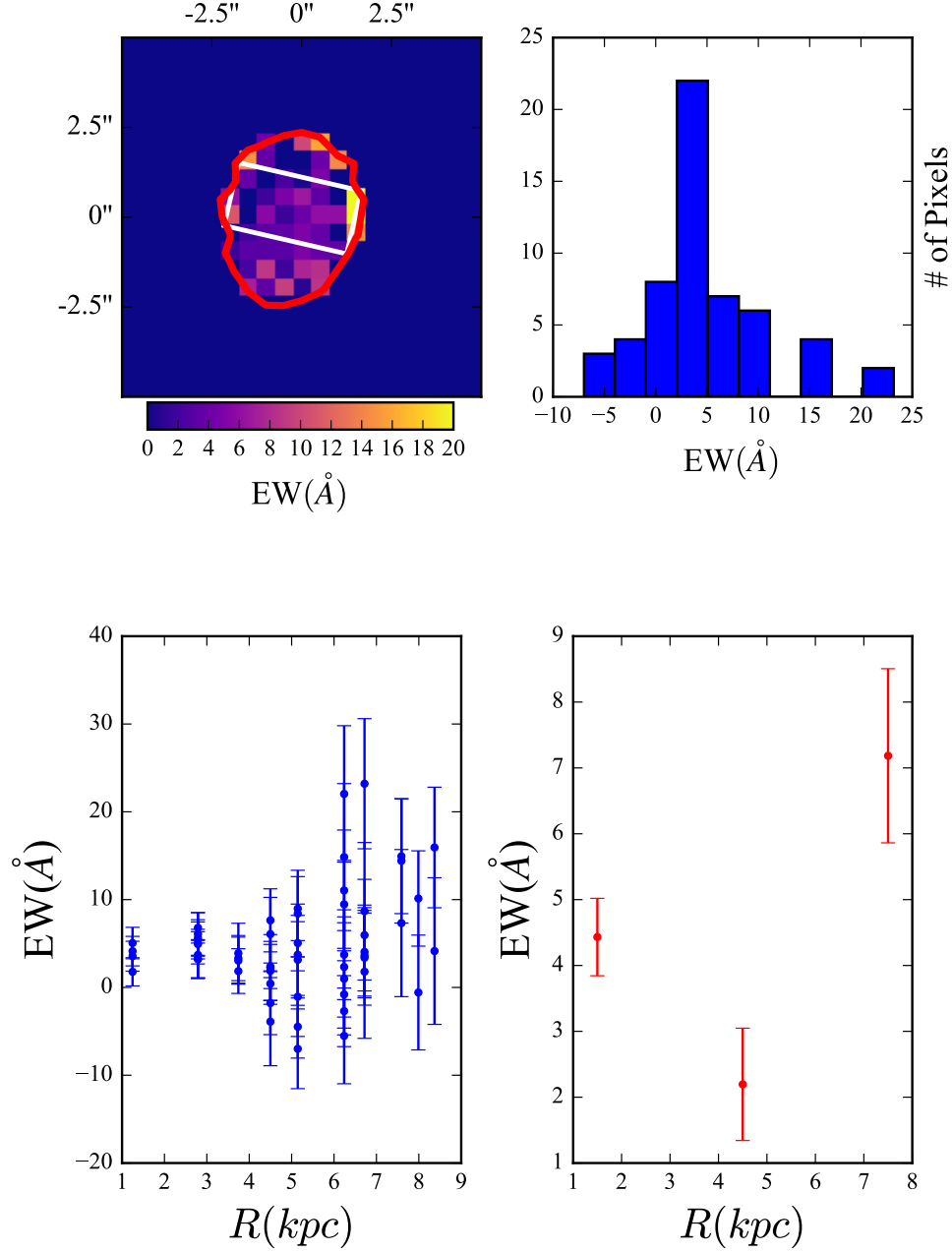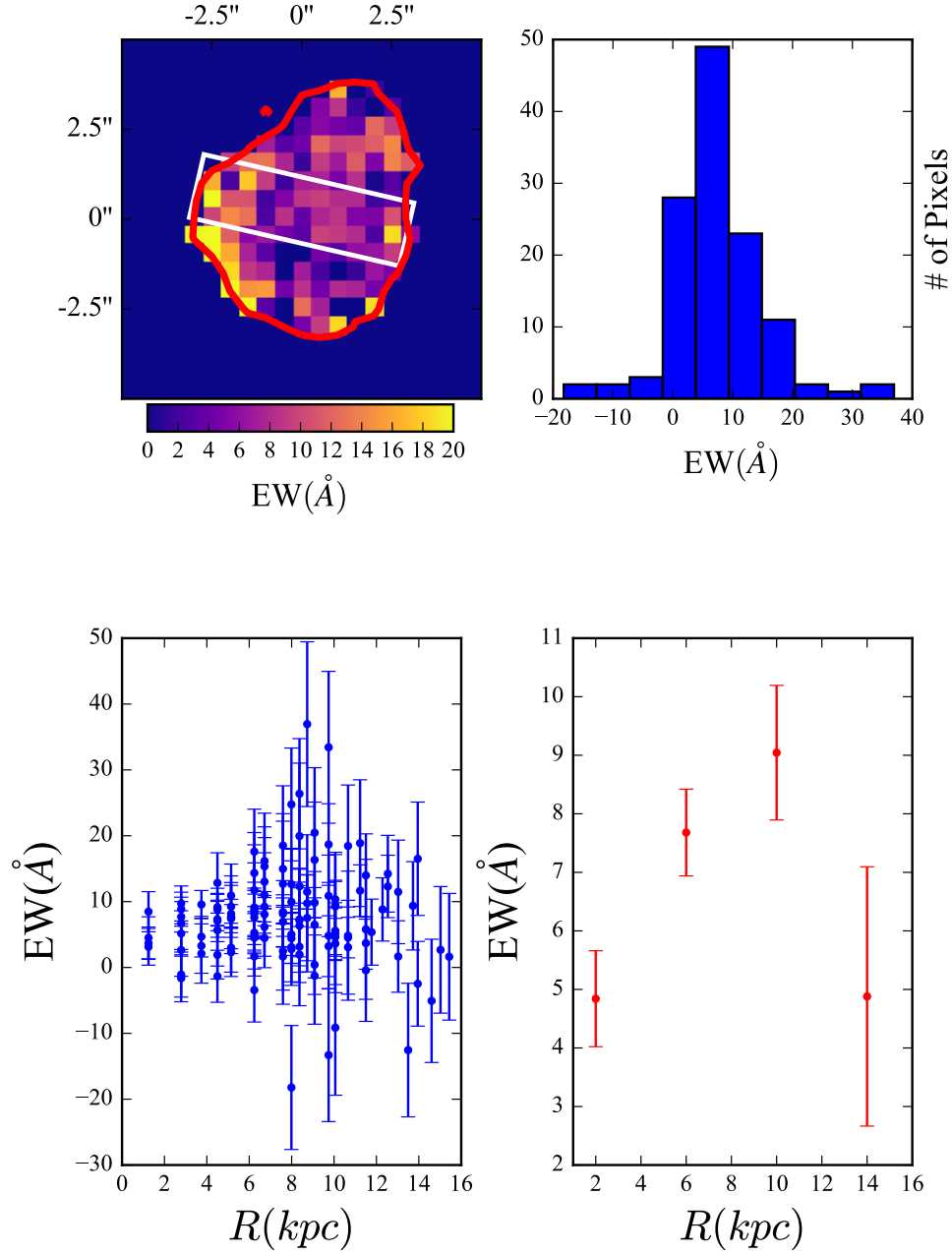
Figure 10. Equivalent width images, distribution and radial projection for J033225.26. (Top Left) image of the Mg II equivalent widths inside the red 1SB$_1$ contour. The white contour represents the 0.9″ wide slit used to measure the equivalent width of absorption in the Keck/LRIS spectra. (Top Right) Distribution of absorption pixels with continuum flux S/N greater than 1.5 inside the slit aperture. (Bottom Left) The EWs of absorption vs projected distance from center. (Bottom Right) Binned EW measurements. Each point represents the mean EW measured in 3 kpc wide bins.
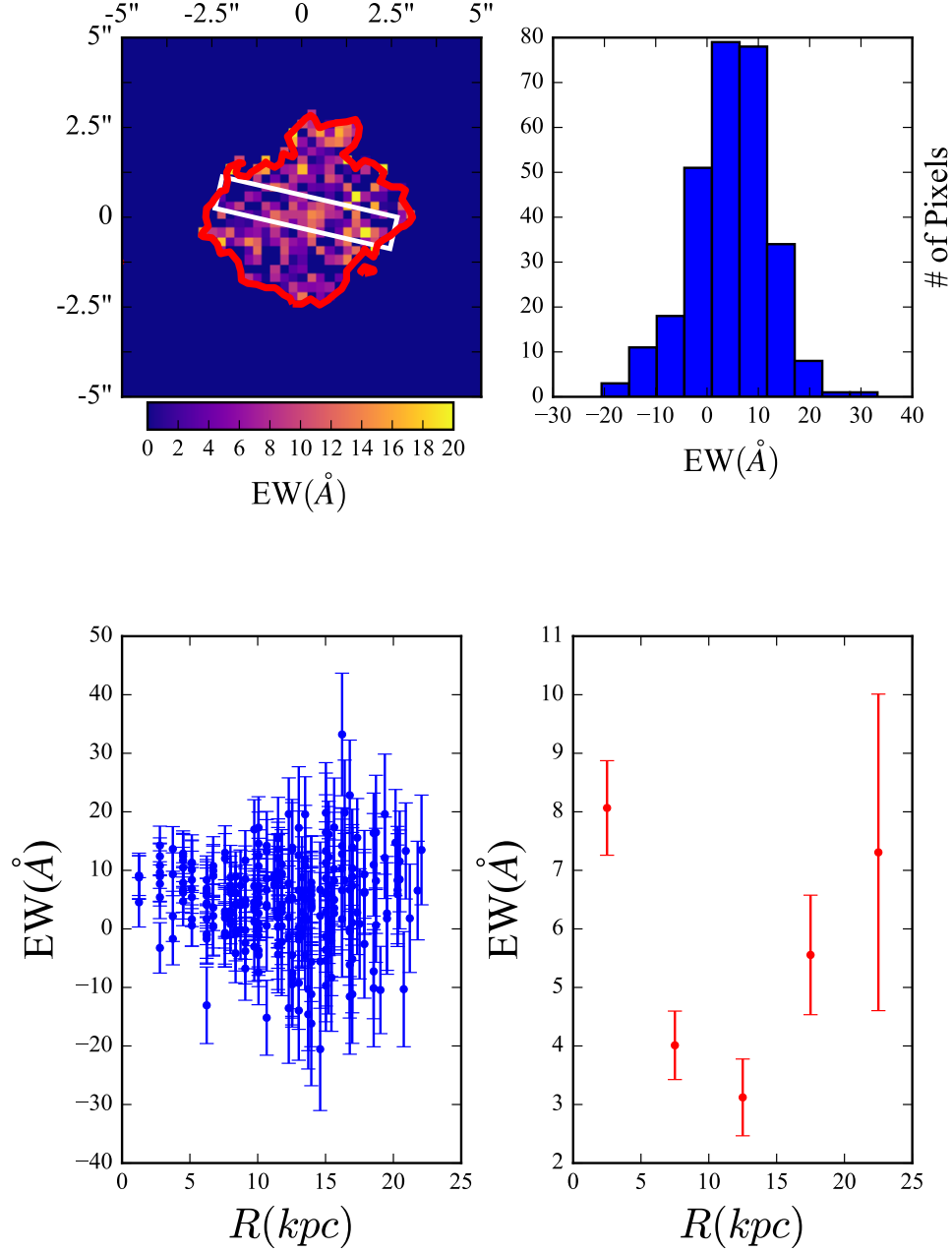
Figure 11. Equivalent width images, distribution and radial projection for J033231.36. (Top Left) image of the Mg II equivalent widths inside the red 1SB$_1$ contour. The white contour represents the 0.9″ wide slit used to measure the equivalent width of absorption in the Keck/LRIS spectra. (Top Right) Distribution of absorption pixels with continuum flux S/N greater than 1.5 inside the slit aperture. (Bottom Left) The EWs of absorption vs projected distance from center. (Bottom Right) Binned EW measurements. Each point represents the mean EW measured in 4 kpc wide bins.

Figure 12. Equivalent width images, distribution and radial projection for J033230.03. (Top Left) Stamp of the equivalent widths (EWs) inside the red $1SB_1$ contour. The white contour represents the $0.9''$ aperture slit used to measure the equivalent width of absorption in the Keck/LRIS spectra. (Top Right) Distribution of absorption pixels with continuum flux S/N greater than 1.5 inside the slit aperture. (Bottom Left) The EWs of absorption projected in distance from center. (Bottom Right) Binned EW measurements. Each point represents the mean EW measured in 5 kpc increment bins.
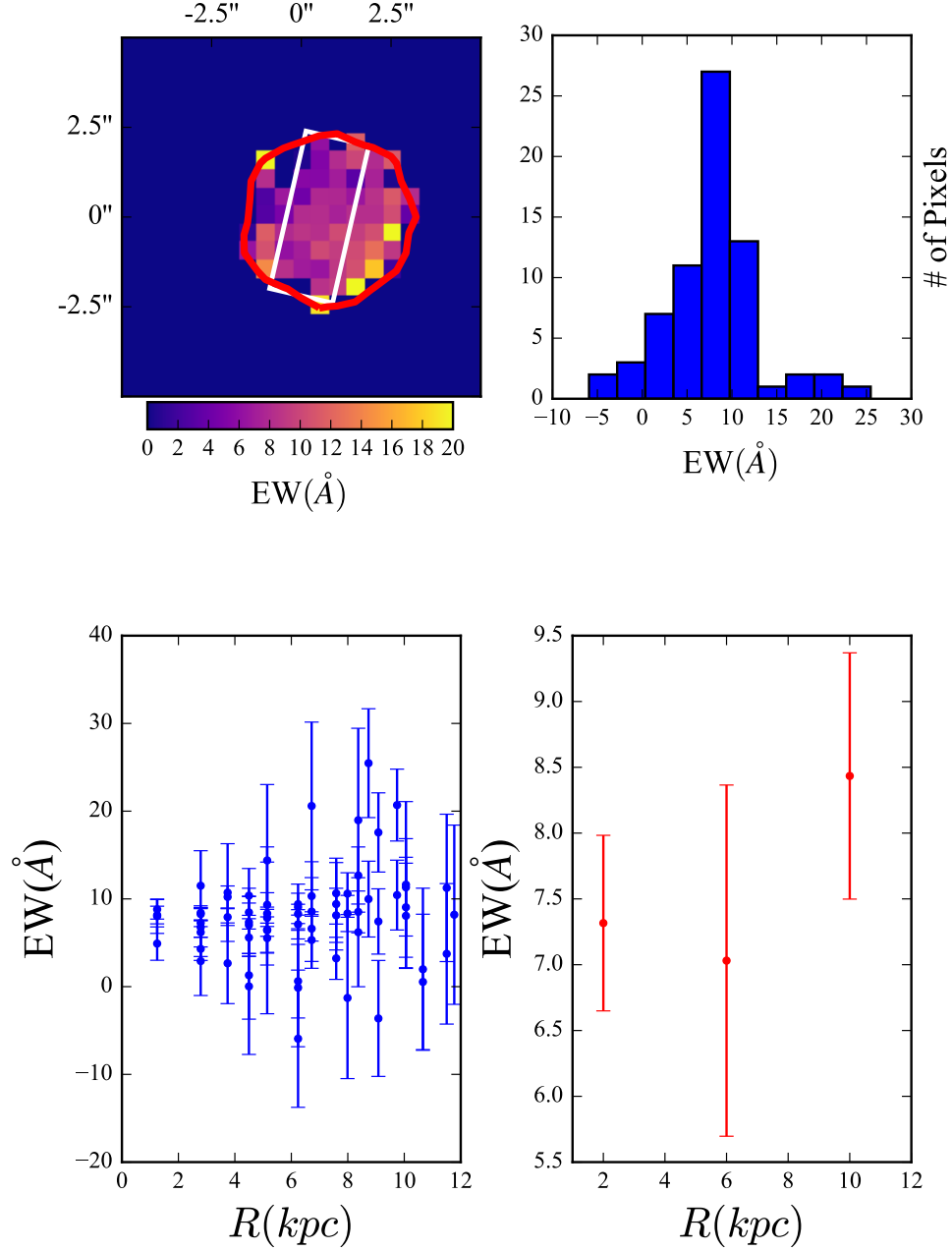
Figure 13. Equivalent width images, distribution and radial projection for J033229.64. (Top Left) Stamp of the equivalent widths (EWs) inside the red $1SB_1$ contour. The white contour represents the $0.9''$ aperture slit used to measure the equivalent width of absorption in the Keck/LRIS spectra. (Top Right) Distribution of absorption pixels with continuum flux S/N greater than 1.5 inside the slit aperture. (Bottom Left) The EWs of absorption projected in distance from center. (Bottom Right) Binned EW measurements. Each point represents the mean EW measured in 4 kpc wide bins.
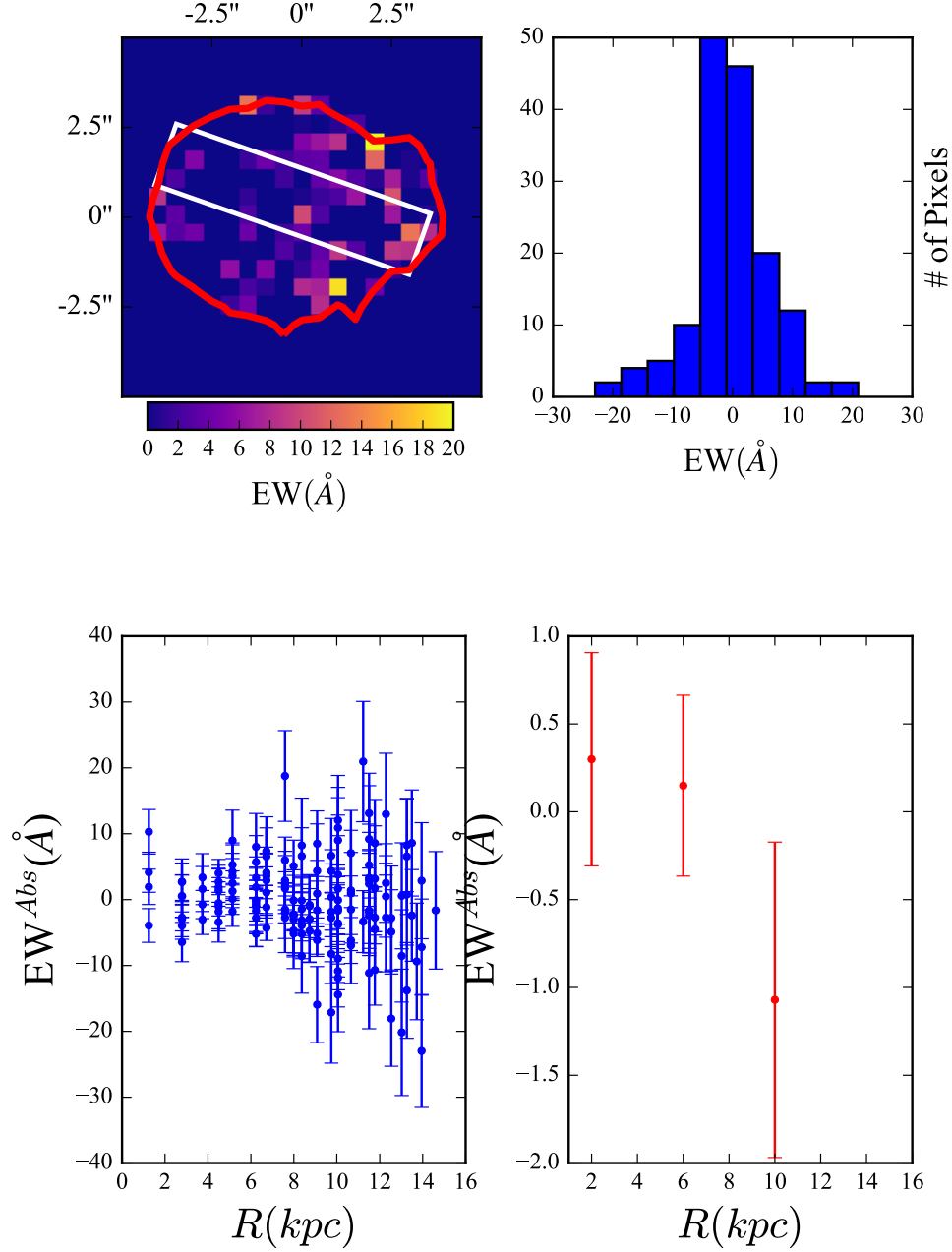
Figure 14. Equivalent width images, distribution and radial projection for J033230.57. (Top Left) Stamp of the equivalent widths (EWs) inside the red $1SB_1$ contour. The white contour represents the $0.9''$ aperture slit used to measure the equivalent width of absorption in the Keck/LRIS spectra. (Top Right) Distribution of absorption pixels with continuum flux S/N greater than 1.5 inside the slit aperture. (Bottom Left) The EWs of absorption projected in distance from center. (Bottom Right) Binned EW measurements. Each point represents the mean EW measured in 4 kpc wide bins.
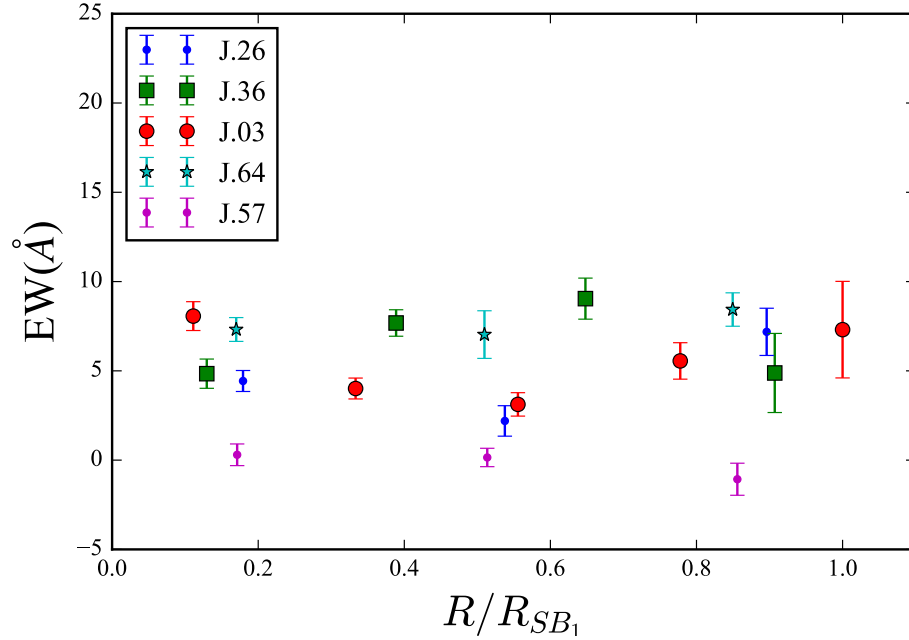
Figure 15. Normalized radial profile of the mean EW of Mg II absorption for all galaxies. Measurements for the mean EW binned in radial increments compiled to test the significance of any trends found in the individual galaxy profiles. There is significant scatter relative to the error bars at extended distances.

REFERENCES

Arrigoni Battaia, F., Yang, Y., Hennawi, J. F., et al. 2015, ApJ, 804, 26

Bertin, E., Mellier, Y., Radovich, M., et al. 1996, A&AS, 117, 393

Chevalier, R. A., & Clegg, A. W. 1985, Nature, 317, 44

Davis, M., Guhathakurta, P., Konidaris, N. P., et al. 2007, ApJL, 660, L1

Erb, D. K., Quider, A. M., Henry, A. L., & Martin, C. L. 2012, ApJ, 759, 26

Giavalisco, M., Ferguson, H. C., Koekemoer, A. M., et al. 2004, ApJL, 600, L93

Hennawi, J. F., & Prochaska, J. X. 2013, ApJ, 766, 58

Kornei, K. A., Shapley, A. E., Martin, C. L., et al. 2013, ApJ, 774, 50

Lang, D., Hogg, D. W., Mierle, K., Blanton, M., & Roweis, S. 2010, AJ, 139, 1782

Larson, R. B. 1974, MNRAS, 169, 229

Martin, C. L., Shapley, A. E., Coil, A. L., et al. 2012, ApJ, 760, 127

Martin, C. L., Shapley, A. E., Coil, A. L., et al. 2013, ApJ, 770, 41

Matsubayashi, K., Sugai, H., Hattori, T., et al. 2009, ApJ, 701, 1636

Prochaska, J. X. 2016, Linetools, https://github.com/linetools/linetools

Prochaska, J. X., Kasen, D., & Rubin, K. 2011, ApJ, 734, 24

Rubin, K. H. R., Prochaska, J. X., Koo, D. C., et al. 2014, ApJ, 794, 156

Rubin, K. H. R., Prochaska, J. X., Ménard, B., et al. 2011, ApJ, 728, 55

Springel, V., & Hernquist, L. 2003, MNRAS, 339, 289

Sugahara, Y., Ouchi, M., Lin, L., et al. 2017, ApJ, 850, 51

Tripp, T. M., Meiring, J. D., Prochaska, J. X., et al. 2011, Science, 334, 952

Veilleux, S., Cecil, G., & Bland-Hawthorn, J. 2005, ARA&A, 43, 769

Veilleux, S., Rupke, D. S. N., & Swaters, R. 2009, ApJL, 700, L149

Weiner, B. J., Coil, A. L., Prochaska, J. X., et al. 2009, ApJ, 692, 187

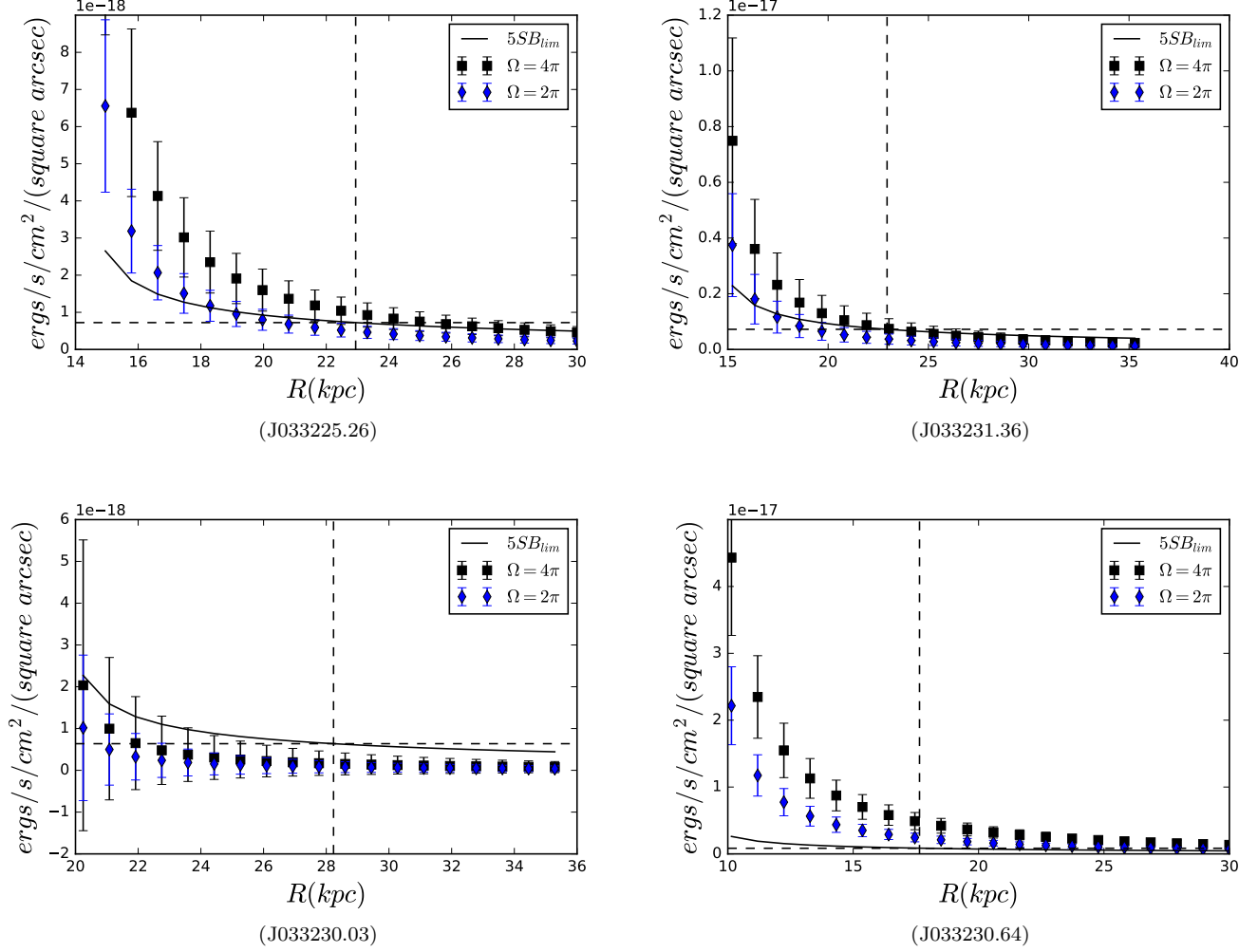Werk, J. K., Prochaska, J. X., Tumlinson, J., et al. 2014, ApJ, 792, 8

Figure 16. Estimated SB profile of Mg II emission for Isotropic and Anisotropic dust-free winds. The black square points are SB of missing Mg II emission uniformly distributed inside an annulus for an angle $\Omega = 4\pi$, or an isotropic wind. The blue diamond points are SB of missing Mg II emission uniformly distributed inside an annulus for an angle $\Omega = 2\pi$, or an anisotropic wind. The solid line shows the value of the SB detection limits. The dashed vertical and horizontal lines represent outer radius of the extended annulus use to measure the initial detection limits and the value of SB detection limit in that annulus.